Icarus 291 (2017) 192–202

Contents lists available at ScienceDirect

Icarus

journal homepage: www.elsevier.com/locate/icarus

A detailed pathway analysis of the chemical reaction system generating the Martian vertical ozone profile

Joachim W. Stock[a,b,*], Christopher S. Blaszczak-Boxe[c,d], Ralph Lehmann[e], J. Lee Grenfell[b,f], A. Beate C. Patzer[f], Heike Rauer[b,f], Yuk L. Yung[g]

[a] Instituto de Astrofísica de Andalucía - CSIC, Glorieta de la Astronomía s/n, 18008 Granada, Spain
[b] Institut für Planetenforschung, Deutsches Zentrum für Luft und Raumfahrt (DLR), Rutherfordstr. 2, 12489 Berlin, Germany
[c] Department of Chemistry and Environmental Science, Medgar Evers College-City University of New York, 1650 Bedford Avenue, Brooklyn, NY 11235, United States
[d] CUNY's Graduate Center's Earth and Environmental Sciences Department and Chemistry Divisions, New York, NY 10016, United States
[e] Alfred-Wegener-Institut, Helmholtz-Zentrum für Polar- und Meeresforschung (AWI), Telegrafenberg A43, 14473 Potsdam, Germany
[f] Zentrum für Astronomie und Astrophysik (ZAA), Technische Universität Berlin (TUB), Hardenbergstr. 36, 10623 Berlin, Germany
[g] Division of Geological and Planetary Sciences, California Institute of Technology, 1200 East California Boulevard, Pasadena, CA 91125, United States

ARTICLE INFO

Article history:
Received 7 December 2015
Revised 15 November 2016
Accepted 5 December 2016
Available online 9 December 2016

Keywords:
Atmospheres chemistry
Atmospheres composition
Mars
Mars atmosphere
Photochemistry

ABSTRACT

Atmospheric chemical composition is crucial in determining a planet's atmospheric structure, stability, and evolution. Attaining a quantitative understanding of the essential chemical mechanisms governing atmospheric composition is nontrivial due to complex interactions between chemical species. Trace species, for example, can participate in catalytic cycles – affecting the abundance of major and other trace gas species. Specifically, for Mars, such cycles dictate the abundance of its primary atmospheric constituent, carbon dioxide (CO_2), but also for one of its trace gases, ozone (O_3). The identification of chemical pathways/cycles by hand is extremely demanding; hence, the application of numerical methods, such as the *Pathway Analysis Program (PAP)*, is crucial to analyze and quantitatively exemplify chemical reaction networks. Here, we carry out the first automated quantitative chemical pathway analysis of Mars' atmosphere with respect to O_3. *PAP* was applied to JPL/Caltech's 1-D updated photochemical Mars model's output data. We determine all significant chemical pathways and their contribution to O_3 production and consumption (up to 80 km) in order to investigate the mechanisms causing the characteristic shape of the O_3 volume mixing ratio profile, i.e. a ground layer maximum and an ozone layer at ~50 km. These pathways explain why an O_3 layer is present, why it is located at that particular altitude and what the different processes forming the near-surface and middle atmosphere O_3 maxima are. Furthermore, we show that the Martian atmosphere can be divided into two chemically distinct regions according to the $O(^3P)$:O_3 ratio. In the lower region (below approximately 24 km altitude) O_3 is the most abundant O_x ($= O_3 + O(^3P)$) species. In the upper region (above approximately 24 km altitude), where the O_3 layer is located, $O(^3P)$ is the most abundant O_x species. Earlier results concerning the formation of O_3 on Mars can now be explained with the help of chemical pathways leading to a better understanding of the vertical O_3 profile.

1. Introduction

Ozone (O_3) is one of the most important chemical species for understanding the chemistry in the carbon dioxide (CO_2) dominated atmosphere of Mars. In the early 1970s McElroy and Donahue (1972) and Parkinson and Hunten (1972) demonstrated that the chemistry, which stabilizes CO_2, is dominated by catalytic cycles involving odd hydrogen ($HO_x = H + OH + HO_2$) species, formed by water vapor (H_2O) photolysis (see also e.g. Atreya and Gu, 1994; Nair et al., 1994; Yung and DeMore, 1999; Stock et al., 2012a,b). Observations and theoretical models of O_3 and H_2O in the Martian atmosphere have clearly shown an anticorrelation between these two molecules (e.g. Lane et al., 1973; Clancy and Nair, 1996; Lefèvre et al., 2004; Montmessin et al., 2004; Smith, 2004; Fast et al., 2006a; Perrier et al., 2006), suggesting that O_3 is a good indicator for extremely low OH and HO_2 volume mixing ratios and

* Corresponding author.
E-mail address: joachimstock14@gmail.com (J.W. Stock).

http://dx.doi.org/10.1016/j.icarus.2016.12.012
0019-1035/

therefore "dry" conditions. Furthermore, O_3 can act in CO_2 forming pathways as a source of atomic oxygen or as a catalyst (Yung and DeMore, 1999; Stock et al., 2012a).

On Mars, atmospheric O_3 was first detected in the southern polar region by ultraviolet (UV) spectrometers aboard Mariner 7 during its flyby in 1969 (Barth and Hord, 1971). Closer investigations of the Hartley O_3 absorption feature at 255 nm wavelength by the Mariner 9 UV spectrometer revealed not only latitudinal and seasonal variations in O_3 concentrations (Barth et al., 1973) but also indicated the above-mentioned anticorrelation between O_3 and H_2O in the atmosphere of Mars (Lane et al., 1973). Noxon et al. (1976) first observed the 1.27 μm $O_2(^1\Delta)$ dayglow emission line in the Martian atmosphere, which results from O_3 photodissociation

$$O_3 + h\nu \longrightarrow O_2(^1\Delta) + O(^1D) \quad (1)$$

emission of a photon

$$O_2(^1\Delta) \longrightarrow O_2(^3\Sigma) + h\nu. \quad (2)$$

Traub et al. (1979) applied this detection method to study and compare O_3 concentrations in the equatorial region between ±20° latitude and the polar regions beyond ±45° latitude. In the following, the 1.27 μm $O_2(^1\Delta)$ dayglow emission has been used to map O_3 and to investigate its seasonal and latitudinal behavior (e.g. Krasnopolsky and Bjoraker, 2000; Novak et al., 2002; Krasnopolsky, 2003). A ground based observational method to measure O_3 directly was introduced by Espenak et al. (1991) using infrared (IR) heterodyne spectroscopy, which provided a higher spatial resolution than $O_2(^1\Delta)$ dayglow observations. IR heterodyne spectra near the 9.7 μm absorption band have been taken with the NASA/Goddard Space Flight Center IRHS (Infrared Heterodyne Spectrometer) and HIPWAC (Heterodyne Instrument for Planetary Wind And Composition) and analyzed by Fast et al. (2006a,b), indicating that the vertical distribution of O_3 plays an important role to understand the deviations from the strict anticorrelation between O_3 and H_2O column integrated abundances (see also Lefèvre et al., 2004).

The early Mars "wet" model of Parkinson and Hunten (1972) already predicted an O_3 concentration layer at an atmospheric height around $z \approx 32$ km. This layer was finally discovered at approximately $z \approx 40$ km altitude by Krasnopolsky et al. (1975) (see also Krasnopolsky and Parshev, 1979), using measurements obtained by the Mars 5 orbiter at the daytime limb and evening terminator. Later solar occultation observations close to the evening terminator near the northern spring equinox by an UV spectrometer aboard the Phobos 2 spacecraft confirmed the existence of the O_3 concentration maximum between $z = 42$ km to $z = 45$ km in the equatorial region (Blamont and Chassefière, 1993).

ESA's Mars Express (MEX) mission led to a significant leap in the exploration of Mars' O_3. Using the UV spectrometer of the SPICAM (SPectroscopy for the Investigation of the Characteristics of the Atmosphere of Mars) instrument (Bertaux et al., 2000, 2006), Lebonnois et al. (2006) and Perrier et al. (2006) measured the vertical and global distribution of O_3, accumulating data from more than one year of observations. This work was supplemented by three dimensional modeling efforts by Lefèvre et al. (2004), who investigated the seasonal, latitudinal and diurnal behavior of O_3 by employing the LMD (Laboratoire de Météorologie Dynamique) GCM (General Circulation Model). Lefèvre et al. (2008) pointed out the potential significance of the heterogeneous chemistry upon ice cloud particles, which act as an effective HO_x sink (resulting in "dryer" conditions), bringing better coincidence between SPICAM O_3 and ground based O_3 and H_2O_2 observations as well as model results. Later observations with the MARCI (MARs Color Imager) instrument onboard MRO (Mars Reconnaissance Orbiter), however, did not provide strong evidence of a correlation between O_3 and clouds (Clancy et al., 2016).

Here, we investigate

(a) why an O_3 layer is present,
(b) why it is located at that particular altitude and
(c) what the different processes forming the near-surface and middle atmosphere ozone maxima are,

by studying how O_3 is produced and consumed on Mars. The problem of explaining direct O_3 production and consumption can be addressed by inspecting calculated reaction rates and searching for the one with the largest rate. However, these reactions can be involved in both fast O_3 null cycles (no net O_3 production or consumption) and catalytic O_3 production or loss pathways. The latter pathways are relevant for explaining the O_3 volume mixing ratio profile. The role of catalytic cycles for O_3 formation and consumption in Earth's atmosphere has been demonstrated by e.g. Bates and Nicolet (1950) and Crutzen (1970). Note, that the presence of catalytic species on Mars has a dramatic impact on the chemical composition of the atmosphere (McElroy and Donahue, 1972; Parkinson and Hunten, 1972), hence it is expected, that catalytic cycles are also relevant to the O_3 formation and consumption on Mars.

Generally, it is very difficult to find a complete set of relevant production and consumption pathways of a given species. Therefore, we use the *Pathway Analysis Program* (*PAP*, Lehmann, 2004), which enables the determination of all dominant pathways in reaction networks. The algorithm has been successfully applied to very different topics such as Earth's stratospheric O_3 (Lehmann, 2004; Grenfell et al., 2006), Earth's mesosphere and ionosphere (Verronen et al., 2011; Verronen and Lehmann, 2013; 2015), the Martian CO_2 stability problem (Stock et al., 2012a,b), and biomarker chemistry on Earth-like extrasolar planets orbiting M-dwarf stars (Grenfell et al., 2013).

Here, we are particularly interested in the shape of the vertical O_3 profile under mean atmospheric conditions and the chemical cycles which determine the location of the O_3 layer. Therefore, we apply for the first time the computer algorithm *PAP* to the output of the updated version of the JPL/Caltech KINETICS model of the Martian atmosphere (Nair et al., 1994; Boxe et al., 2014) to identify all significant chemical pathways and quantify their contribution to O_3 formation and consumption up to 80 km altitude.

2. Method

2.1. Martian atmospheric photochemical column model

To study the O_3 profile in the Martian atmosphere under global average conditions with the help of the *Pathway Analysis Program* (*PAP*, Lehmann, 2004), the output of the updated version of the JPL/Caltech Martian atmospheric photochemical column model has been employed, which was described in detail by Nair et al. (1994). The version of the photochemical kinetics model used here provides the mathematical solution of a system of coupled one-dimensional continuity equations

$$\frac{\partial}{\partial t} n_i(z,t) + \frac{\partial}{\partial z}\Phi_i(z,t) = \mathcal{P}_i(n_1,\ldots,n_{N_S}) - \mathcal{L}_i(n_1,\ldots,n_{N_S}) \quad (3)$$

for $N_S = 29$ species ($O(^3P)$, $O(^1D)$, $O_2(^3\Sigma)$, $O_2(^1\Delta)$, O_3, $N(^4S)$, $N(^2D)$, N_2, N_2O, NO, NO_2, NO_3, N_2O_5, HNO_2, HNO_3, HO_2NO_2, H, H_2, H_2O, OH, HO_2, H_2O_2, CO, CO_2, HCO_2, O^+, O_2^+, CO_2^+, CO_2H^+), where z denotes the atmospheric altitude, $\mathcal{P}_i(n_1,\ldots,n_{N_S})$ the production rate and $\mathcal{L}_i(n_1,\ldots,n_{N_S})$ the loss rate of species S_i with the related number density n_i. The vertical flux of species S_i is calculated via

$$\Phi_i = -D_i\left(\frac{dn_i}{dz} + \frac{n_i}{H_i} + \frac{n_i(1+\alpha_i)}{T}\frac{dT}{dz}\right) - K\left(\frac{dn_i}{dz} + \frac{n_i}{H} + \frac{n_i}{T}\frac{dT}{dz}\right), \quad (4)$$

where D_i, H_i and α_i are the molecular diffusion coefficient, the scale height and the thermal diffusion factor of species S_i, respectively. K, H, and T denote the eddy diffusion coefficient, the scale height of the background atmosphere and the local gas temperature, respectively. The vertical grid covers the atmosphere from the Martian surface up to 240 km in 2 km intervals. For the chemical pathway analysis, we used the steady state solution of the photochemical model for fixed temperature and pressure profiles (for details see Nair et al., 1994). The chemical reaction system includes 149 reactions (for details see Stock et al., 2012a; Boxe et al., 2014). In contrast to Stock et al. (2012a), we distinguish between the excited state $O_2(^1\Delta)$ and the ground state $O_2(^3\Sigma)$ of molecular oxygen. Additionally, the HCO_2 chemistry introduced by Boxe et al. (2014) is included in the chemical model. Reaction rate coefficients are updated according to Sander et al. (2011).

Since the O_3 volume mixing ratio exhibits latitudinal, diurnal and seasonal variations, the utilization of one-dimensional models is limited. For example, horizontal transport cannot be described, i.e. the effect of atmospheric circulation is parameterized within the eddy diffusion profile, which is derived from aerosol measurements (see Nair et al., 1994, and references therein). Nevertheless, in order to discuss the O_3 chemistry under global mean conditions, it is useful to abstain from the three-dimensional treatment in favor of a more detailed description of the chemical reaction network. This approach is strengthened by the fact, that the results of the O_3 volume mixing ratio profile calculated with the help of the JPL/Caltech photochemical model are within observational constraints (Nair et al., 1994).

For the description of the photolysis rate constants a diurnally averaged solar radiation field for ca. 30° latitude at equinox is assumed. The diurnally averaged radiation corresponds to the radiation at 7:15 a.m. LTST (local true solar time) and 4:45 p.m. LTST. It is well known that the O_3 concentration in the O_3 layer considerably varies diurnally since the chemical lifetime of O_3 is shorter than one day (see e.g. Nair et al., 1994; Lefèvre et al., 2004; Perrier et al., 2006). Note, that although we assume a diurnally averaged radiation field, the resulting O_3 concentration does not necessarily represent the diurnally averaged O_3 concentration.

The eddy diffusion profile is given by Nair et al. (1994), their Fig. 1(b). The eddy diffusion coefficient (K) is $10^5\,cm^2s^{-1}$ at the surface and increases exponentially up to $10^7\,cm^2s^{-1}$ at $z = 40$ km consistent with aerosol measurements (Toon et al., 1977; Anderson and Leovy, 1978; Chassefière et al., 1992; Korablev et al., 1993). Between $z = 40$ km and $z = 70$ km, K is constant. The value is chosen to reproduce the O_2 volume mixing ratio as discussed by Nair et al. (1994). Rosenqvist and Chassefière (1995) reexamined the relationship between eddy mixing and O_2 concentration, which is consistent with the value of the eddy diffusion coefficient used here. Between $z = 70$ km and $z = 100$ km, the eddy diffusion coefficient increases again exponentially with increasing altitude up to $K = 10^8\,cm^2s^{-1}$ to match the abundance of atomic oxygen at the thermosphere.

Water vapor (H_2O) is the most important reservoir species for HO_x radicals. Its abundance on Mars is mainly controlled by condensation/evaporation and the global circulation and consequently exhibits diurnal, seasonal and latitudinal variations (see for example Barker, 1976; Jakosky and Farmer, 1982; Jakosky, 1985; Houben et al., 1997; Richardson and Wilson, 2002; Montmessin et al., 2004). However, one-dimensional models generally use fixed water profiles. Here we utilize the standard H_2O profile employed by Nair et al. (1994) in order to represent mean conditions, i.e. we assume a well mixed water abundance in the lower atmosphere up to the hygropause, the height where H_2O becomes saturated. Above $z \approx 60$ km, where the H_2O saturation profile has a minimum, H_2O is undersaturated and its abundance is determined by photochemistry.

2.2. Pathway Analysis Program

The *Pathway Analysis Program (PAP)* allows for the identification of chemical pathways in arbitrarily given reaction networks. Additionally, it quantifies the efficiency of the pathways by computing the corresponding rates. In this way, the relative importance of the different, competing chemical pathways can be determined. *PAP* was described in more detail by Lehmann (2004) and some applications with respect to the CO_2 formation on Mars were discussed by Stock et al. (2012a,b).

In accordance with Stock et al. (2012a) we denote the rate of the net change of species S_i caused by pathway P_k by

$$\varphi_{ik} = |m_{ik}| f_k, \qquad i = 1, \ldots, N_S, \;\; k = 1, \ldots, N_P, \quad (5)$$

where m_{ik} is the stoichiometric coefficient of species S_i in the net reaction of pathway P_k with its rate f_k. N_P is the total number of pathways.

In order to identify the chemical pathways in the Martian atmosphere and to quantify their efficiencies, we apply the *PAP* algorithm to the steady-state solution of the JPL/Caltech KINETICS model for each atmospheric layer separately (see Stock et al., 2012a, for further details).

In general, chemical production $\mathcal{P}_i$ and chemical consumption $\mathcal{L}_i$ in planetary atmospheres can differ even under steady state conditions if other sources or sinks apart from chemical reactions are present – such as for instance vertical diffusion (see Eq. (3)). The analysis method can be extended to account for such processes by introducing pseudo reactions describing emission, transport processes etc. Since $O(^3P)$ is strongly affected by vertical transport, we include two pseudo reactions:

$$O(^3P)[\text{adjacent layer(s)}] \longrightarrow O(^3P) \quad (6)$$

$$O(^3P) \longrightarrow O(^3P)[\text{adjacent layer(s)}], \quad (7)$$

representing the transport into or out of a layer centered at altitude z.

We calculate the associated reaction rates under steady state conditions (i.e. $\partial n_{O(^3P)}/\partial t = 0$) by using Eq. (3) and treating the term $\partial \Phi_{O(^3P)}/\partial z$ according to its sign as a *pseudo production rate*

$$r^{\text{gain}}_{O(^3P)} = \begin{cases} -\partial \Phi_{O(^3P)}/\partial z, & \partial \Phi_{O(^3P)}/\partial z < 0 \\ 0, & \text{otherwise} \end{cases} \quad (8)$$

or a *pseudo consumption rate*

$$r^{\text{loss}}_{O(^3P)} = \begin{cases} \partial \Phi_{O(^3P)}/\partial z, & \partial \Phi_{O(^3P)}/\partial z > 0 \\ 0, & \text{otherwise.} \end{cases} \quad (9)$$

There are several O_3 photolysis channels leading to ground state atomic oxygen $O(^3P)$, electronically excited state of atomic oxygen ($O(^1D)$), ground state molecular oxygen $O_2(^3\Sigma)$ and/or electronically excited molecular oxygen ($O_2(^1\Delta)$) (see Matsumi et al., 2002, for example). The most important ones in the Martian atmosphere are the spin-allowed channels (1) and

$$O_3 + h\nu \longrightarrow O_2(^3\Sigma) + O(^3P). \quad (10)$$

Another considerable source of $O(^3P)$ and $O(^1D)$ are the photolysis of CO_2

$$CO_2 + h\nu \longrightarrow CO + O(^3P) \quad (11)$$

$$\longrightarrow CO + O(^1D) \quad (12)$$

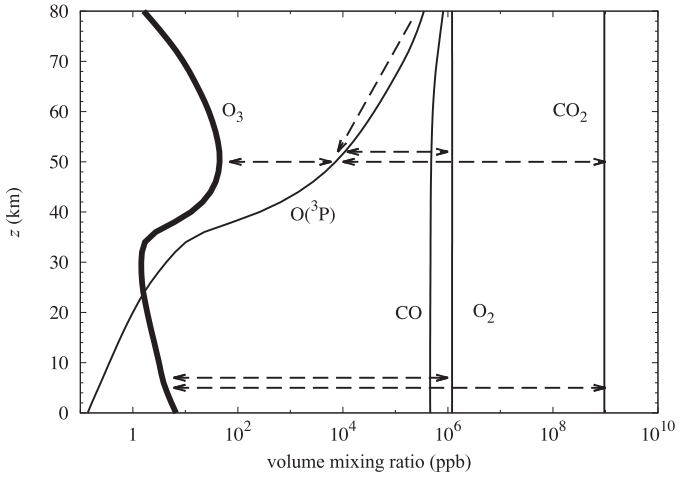

(a) Odd oxygen (O(3*P*), O3), molecular oxy-gen (O2), carbon monoxide (CO), carbon dioxide(CO2))

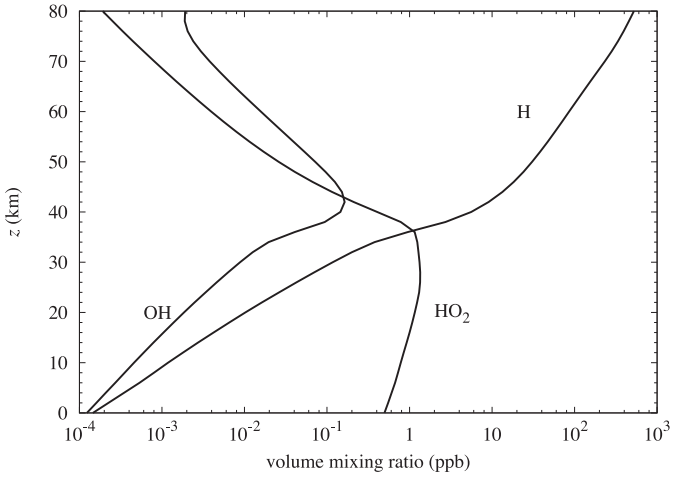

(b) Odd hydrogen species (H, OH, HO2).

Fig. 1. Volume mixing ratios of selected atomic and molecular species in the Martian atmosphere calculated by the Caltech/JPL KINETICS model. Dashed arrows in the left hand panel indicate the exchange of oxygen atoms between species. There are one long-lived source of O_3 above $z \approx 24$ km, namely $O(^3P)$ and two long-lived sources of O_3 below $z \approx 24$ km, namely O_2 and CO_2. The processes are explained in more detail in Sections 3.2 and 3.3.

and of $O_2(^3\Sigma)$

$$O_2(^3\Sigma) + h\nu \longrightarrow O(^3P) + O(^3P) \tag{13}$$

$$\longrightarrow O(^3P) + O(^1D) \tag{14}$$

with different reaction channels. The collisional deactivation of $O(^1D)$

$$O(^1D) + CO_2 \longrightarrow O(^3P) + CO_2 \tag{15}$$

and of $O_2(^1\Delta)$

$$O_2(^1\Delta) + CO_2 \longrightarrow O_2(^3\Sigma) + CO_2 \tag{16}$$

with the most abundant species in the Martian atmosphere are relatively fast, especially in the lower atmospheric parts. As a result, the combinations {(1), (15), (16)}, {(12), (15)} and {(14), (15)} may occur within the pathways found by the *PAP* algorithm. As {(1)} has the same net effect as reaction (10), for each pathway P containing the reactions (1), (15) and (16), there exists a competing pathway P' containing the set of reactions as P, but with reaction (10) instead of the reactions (1), (15) and (16). Analogously, for each pathway P containing the reactions (12) and (15) there is a competing pathway P' containing the set of reactions as P, but with reaction (11) instead of the reactions (12) and (15). Since the different photolysis channels are not relevant for the analysis, we simplify the representation of the pathways containing different photolysis channels by merging the pathways P and P' into pathway families. In other words, we distinguish between electronically excited and ground state atoms/molecules, when running the JPL/Caltech KINETICS model and the *PAP*, but introduce a simplified notation, using the "$\Longrightarrow$"-symbol, if several reaction channels with and without subsequent quenching are relevant, when discussing the results of the *PAP*.

2.3. Additional definitions

Ozone can be recycled by null pathways, for instance

$$\begin{array}{rcl} O_3 + h\nu & \Longrightarrow & O_2(^3\Sigma) + O(^3P) \\ O(^3P) + O_2(^3\Sigma) + CO_2 & \longrightarrow & O_3 + CO_2 \\ \hline \text{net:} \qquad \text{null.} & & \end{array} \tag{17}$$

which do not change directly the O_3 concentration. Hence, for explaining the O_3 concentration, it is useful to eliminate their effect from the production and consumption rates of O_3 Therefore, we distinguish the rate of null pathways

$$\hat{\mathcal{N}}_i = \sum_{\{k|m_{ik}=0\}}^{N_P} \tilde{m}_{ik} f_k \tag{18}$$

recycling S_i=O_3 $\tilde{m}_{ik} \in \mathbb{N}$ times in pathway P_k from the rate of production

$$\hat{\mathcal{P}}_i = \sum_{\{k|m_{ik}>0\}}^{N_P} m_{ik} f_k \tag{19}$$

by chemical pathways forming S_i=O_3 from long-lived oxygen reservoir species like CO_2 and O_2 and from the rate of consumption

$$\hat{\mathcal{L}}_i = \sum_{\{k|m_{ik}<0\}}^{N_P} |m_{ik}| f_k \tag{20}$$

by chemical pathways converting $S_i = O_3$ to long-lived oxygen reservoir species. Since the rate of each reaction is completely distributed to the pathways P_k, including null pathways, it follows directly that

$$\mathcal{P}_i = \hat{\mathcal{P}}_i + \hat{\mathcal{N}}_i \tag{21}$$

$$\mathcal{L}_i = \hat{\mathcal{L}}_i + \hat{\mathcal{N}}_i. \tag{22}$$

To ease the discussion of our results, we define the production rate by reactions and by chemical pathways in volume mixing ratio

$$\mathscr{P}_i(z) := \frac{\mathcal{P}_i(z)}{n_{\text{tot}}(z)} \tag{23}$$

$$\hat{\mathscr{P}}_i(z) := \frac{\hat{\mathcal{P}}_i(z)}{n_{\text{tot}}(z)}, \tag{24}$$

where

$$n_{\text{tot}}(z) = \sum_{i=1}^{N_S} n_i(z) \tag{25}$$

is the altitude dependent total number density.

Since steady state conditions ($\partial n_i(z,t)/\partial t = 0$) are assumed and the change in volume mixing ratio of $S_i = O_3$ by vertical transport is relatively small in comparison to the change in volume mixing ratio by chemical production or loss (about $\lesssim$ 1% in the altitude

regions which contain the O_3 maxima), the term $\partial\Phi_i(z, t)/\partial z$ in Eq. (3) can be neglected and it follows

$$\mathcal{P}_i(z) = \mathcal{L}_i(z). \tag{26}$$

Using Eqs. (21), (22) and (26) we find

$$\hat{\mathcal{P}}_i(z) = \hat{\mathcal{L}}_i(z). \tag{27}$$

As a measure of how fast a species S_i undergoes chemical loss reactions, it is useful to define the pseudo first order loss rate coefficient[1]

$$\Lambda_i(z) := \frac{\mathcal{L}_i(z)}{n_i(z)}. \tag{28}$$

Thus the steady state volume mixing profiles can be expressed by

$$\frac{n_i(z)}{n_{\text{tot}}(z)} = \frac{\mathscr{P}_i(z)}{\Lambda_i(z)}, \tag{29}$$

using Eqs. (23), (26) and (28). Although Eq. (29) is formally correct, the right hand side depends on $S_i = O_3$, since $\mathscr{P}_i(z)$ and $\Lambda_i(z)$ contain the rate of null pathways (see Eqs. (21)–(23) and (28)). This means both sides of Eq. (29) depend on $S_i = O_3$ and hence this equation is not helpful for explaining the mechanisms generating the O_3 volume mixing ratio profile. Therefore, in analogy to Eq. (28) we define

$$\hat{\Lambda}_i(z) := \frac{\hat{\mathcal{L}}_i(z)}{n_i(z)} \tag{30}$$

Thus the steady state volume mixing profiles can also be expressed by

$$\frac{n_i(z)}{n_{\text{tot}}(z)} = \frac{\hat{\mathscr{P}}_i(z)}{\hat{\Lambda}_i(z)} \tag{31}$$

using Eqs. (24), (30) and (27).

3. Results and discussion

3.1. The O_3 volume mixing ratio profile

Fig. 1(a) shows among others the vertical profile of O_3 as calculated by the updated version of the Caltech/JPL KINETICS model for the Martian atmosphere. The O_3 volume mixing ratio profile exhibits two maxima: one near the Martian surface, henceforth called *ground layer O_3 maximum*, and another one at an atmospheric height around $z = 50$ km altitude (corresponding to a concentration maximum at $z \approx 44$ km), henceforth *O_3 layer*. Fig. 1(a) also shows the volume mixing ratio of $O(^3P)$, which increases monotonically with increasing altitude. The profiles of $O(^3P)$ and O_3 intersect at about $z \approx 24$ km. Consequently, we find two distinct chemical regions: The lower region ($n_{O(^3P)} < n_{O_3}$) contains the ground layer O_3 maximum. Here, the O_3 abundance is directly controlled by the reservoir species CO_2 and O_2 (indicated by the lower two arrows in Fig. 1(a)). The upper region ($n_{O(^3P)} > n_{O_3}$) includes the O_3 layer. Here, the O_3 concentration is controlled by $O(^3P)$, which in turn is regulated by CO_2 and O_2 (indicated by the upper two horizontal arrows in Fig. 1(a)) and transport (indicated by the diagonal arrow in Fig. 1(a)). Both regions are chemically quite different (see below) and will be analyzed separately.

3.2. Chemical O_3 pathways in the lower region

To understand the shape of the O_3 profile in the lower region, Fig. 2 shows production rates $\mathscr{P}_{O_3}(z)$ and $\hat{\mathscr{P}}_{O_3}(z)$, as well as the first order pseudo loss rate coefficients $\Lambda_{O_3}(z)$ and $\hat{\Lambda}_{O_3}(z)$. Due to

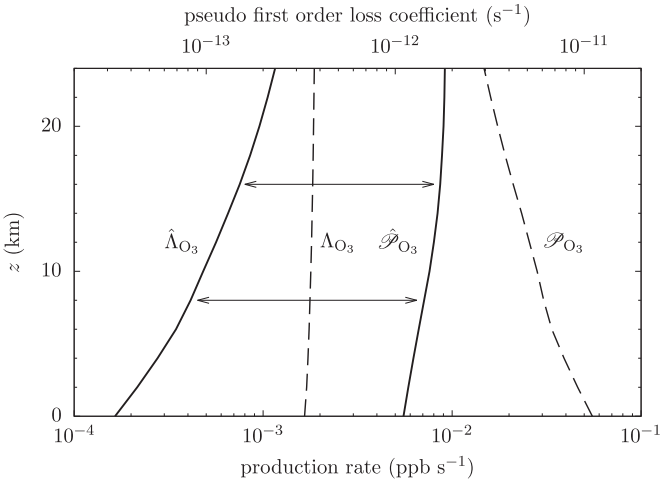

Fig. 2. Pseudo first order O_3 loss rate coefficients Λ_{O_3} and $\hat{\Lambda}_{O_3}$ (left hand side, upper axis) and O_3 production rates $\mathscr{P}_{O_3}$ and $\hat{\mathscr{P}}_{O_3}$ (right hand side, lower axis) in the lower region. Solid lines refer to the production rate $\hat{\mathscr{P}}_{O_3}$ and pseudo first order loss rate coefficient $\hat{\Lambda}_{O_3}$ via pathways according to Eqs. (24) and (30). Dashed lines refer to the production rate $\mathscr{P}_{O_3}$ and pseudo first order loss rate coefficient Λ_{O_3} via reactions. Since the x-axis is in logarithmic scale, the difference between the solid lines, indicated by the length of the horizontal arrows, describes the ratio $\hat{\mathscr{P}}_{O_3} : \hat{\Lambda}_{O_3}$, which is the volume mixing ratio of O_3 according to Eq. (31).

the significant amount of O_3 recycled via pathway (17) in the lower region it follows that $\mathscr{P}_{O_3}(z) \gg \hat{\mathscr{P}}_{O_3}(z)$ and $\Lambda_{O_3}(z) \gg \hat{\Lambda}_{O_3}(z)$ (see Section 2.3). In the logarithmic plot (Fig. 2), the lengths of the arrows correspond to the O_3 volume mixing ratio (see also Eq. (31)). In the lower region, $\hat{\mathscr{P}}_{O_3}(z)$ decreases about a factor of two with decreasing altitude, while $\hat{\Lambda}_{O_3}(z)$ decreases about a factor of seven with decreasing altitude, indicating that the ground layer O_3 maximum is caused by the decrease of the $\hat{\Lambda}_{O_3}$ with decreasing altitude (see Eq. (31)). The relative contributions of all pathways consuming/forming O_3 in the lower region are shown in detail in Fig. 3 and will be discussed in the following sections.

3.2.1. Ozone production (lower region)

Figure 3 and Table 1 show that the majority of O_3 in the lower region is formed via a *Chapman-like* O_3 production pathway

$$\begin{array}{rrcl} & CO_2 + h\nu & \longrightarrow & CO + O(^3P) \\ & O(^3P) + O_2(^3\Sigma) + M & \longrightarrow & O_3 + M \\ \text{net:} & O_2(^3\Sigma) + CO_2 & \longrightarrow & O_3 + CO, \end{array} \tag{32}$$

i.e. $O(^3P)$, which reacts with $O_2(^3\Sigma)$ to produce O_3, is formed by CO_2 photolysis and M is CO_2. The original Chapman O_3 production pathway

$$\begin{array}{rrcl} & O_2(^3\Sigma) + h\nu & \longrightarrow & O(^3P) + O(^3P) \\ & 2 \cdot (O(^3P) + O_2(^3\Sigma) + M & \longrightarrow & O_3 + M) \\ \text{net:} & 3 \cdot O_2(^3\Sigma) & \longrightarrow & 2 \cdot O_3 \end{array} \tag{33}$$

– well known for operating in Earth's atmosphere (M is N_2 or O_2) yielding the notable O_3 layer – is also active on Mars with M = CO_2. However, on Mars, pathway (33) is less efficient than pathway (32), because of the large CO_2:O_2 ratio in the Martian atmosphere. The O_3 production decreases with decreasing altitude, because of the decreasing rates of the CO_2 and O_2 photolysis reactions with decreasing altitude. Furthermore, we identify another

[1] Sometimes called the implicit loss coefficient (see e.g. Jacobson, 2005).

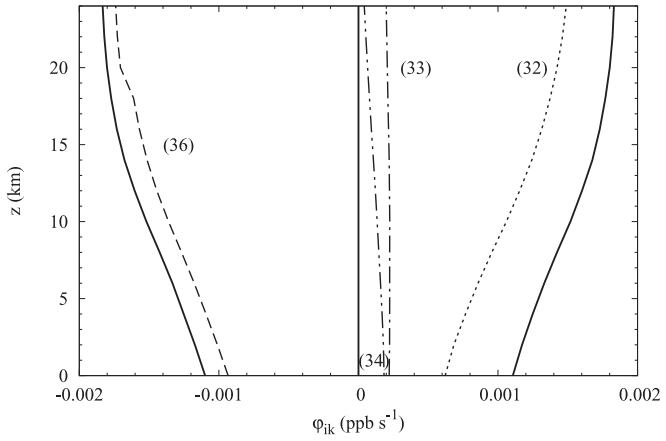

Fig. 3. Rates φ_{ik} of O_3 production/consumption pathways in the lower region. Loss rates are indicated with a negative sign. The solid line on the right hand side indicates the production of O_3 by all O_3 formation pathways. The solid line on the left hand side indicates the consumption of O_3 by all O_3 consumption pathways. Bracketed numbers refer to pathways given in the text and Table 1.

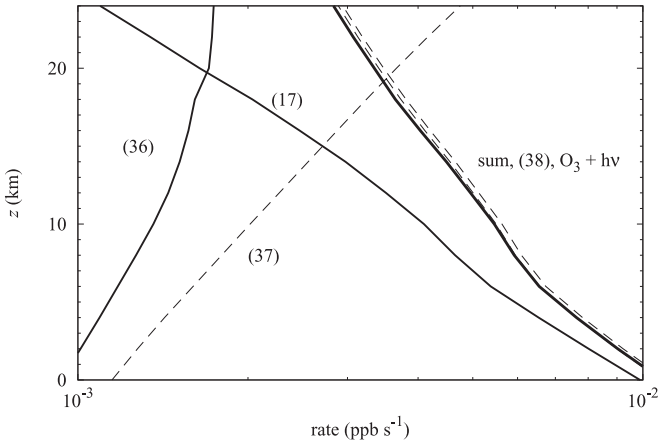

Fig. 4. Rates φ_{ik} of the dominant O_3 consumption pathway family (36) and the null pathway family (17) in the lower region (solid lines). Dashed lines refer to reactions (37), (38) and the photolysis $O_3 + h\nu \Longrightarrow O_2(^3\Sigma) + O(^3P)$. The sum of the pathway family (36) and (17) is indicated by the bold solid line.

Table 1
Percentage contribution of the dominant O_3 production and consumption pathways at the O_3 ground layer maximum.

Production		
(32)	$CO_2 + h\nu \longrightarrow CO + O(^3P)$ $O(^3P) + O_2(^3\Sigma) + M \longrightarrow O_3 + M$	
Net:	$O_2(^3\Sigma) + CO_2 \longrightarrow O_3 + CO$	**56%**
(33)	$O_2(^3\Sigma) + h\nu \longrightarrow O(^3P) + O(^3P)$ $2\cdot(\ O(^3P) + O_2(^3\Sigma) + M \longrightarrow O_3 + M\ )$	
Net:	$3\cdot O_2(^3\Sigma) \longrightarrow 2\cdot O_3$	**20%**
(34)	$OH + CO \longrightarrow CO_2 + H$ $H + O_2(^3\Sigma) + M \longrightarrow HO_2 + M$ $HO_2 + NO \longrightarrow NO_2 + OH$ $NO_2 + h\nu \longrightarrow NO + O(^3P)$ $O(^3P) + O_2(^3\Sigma) + M \longrightarrow O_3 + M$	
Net:	$2\cdot O_2(^3\Sigma) + CO \longrightarrow O_3 + CO_2$	**17%**
Consumption		
(36)	$O_3 + h\nu \Longrightarrow O_2(^3\Sigma) + O(^3P)$ $O(^3P) + HO_2 \longrightarrow OH + O_2(^3\Sigma)$ $OH + CO \longrightarrow CO_2 + H$ $H + O_2(^3\Sigma) + M \longrightarrow HO_2 + M$	
Net:	$O_3 + CO \longrightarrow O_2(^3\Sigma) + CO_2$	**85%**

significant O_3 production pathway

$$\begin{array}{rrl} & OH + CO & \longrightarrow CO_2 + H \\ & H + O_2(^3\Sigma) + M & \longrightarrow HO_2 + M \\ & HO_2 + NO & \longrightarrow NO_2 + OH \\ & NO_2 + h\nu & \longrightarrow NO + O(^3P) \\ & O(^3P) + O_2(^3\Sigma) + M & \longrightarrow O_3 + M \\ \text{net:} & 2\cdot O_2(^3\Sigma) + CO & \longrightarrow O_3 + CO_2, \end{array} \tag{34}$$

which includes the reaction

$$HO_2 + NO \longrightarrow NO_2 + OH \tag{35}$$

reconsidered by Krasnopolsky (1993), who recognized its importance in breaking the O_2 bond to produce odd oxygen. Pathway (34) was already discussed by Stock et al. (2012b) but in the context of CO_2 formation on Mars. This pathway is also relevant for the CO oxidation and O_3 formation in Earth's troposphere (Brasseur et al., 1999) with M being N_2 or O_2 instead of CO_2.

3.2.2. Ozone consumption (lower region)

The dominant O_3 removal process belongs to the pathway family

$$\begin{array}{rrl} & O_3 + h\nu & \Longrightarrow O_2(^3\Sigma) + O(^3P) \\ & O(^3P) + HO_2 & \longrightarrow OH + O_2(^3\Sigma) \\ & OH + CO & \longrightarrow CO_2 + H \\ & H + O_2(^3\Sigma) + M & \longrightarrow HO_2 + M \\ \text{net:} & O_3 + CO & \longrightarrow O_2(^3\Sigma) + CO_2, \end{array} \tag{36}$$

(see Section 2.2 for the definition of the "$\Longrightarrow$"-symbol) the rate of which decreases with decreasing altitude (see Fig. 3). This decrease is a result of increasing competition with the null pathway family (17) for $O(^3P)$ produced by the O_3 photolysis reaction (see Fig. 4). The rate of the O_3 photolysis reaction is almost completely distributed to the pathway families (17) and (36). It is therefore sufficient to examine the ratio of the reactions

$$O(^3P) + HO_2 \longrightarrow OH + O_2(^3\Sigma) \tag{37}$$

and

$$O(^3P) + O_2(^3\Sigma) + CO_2 \longrightarrow O_3 + CO_2. \tag{38}$$

The ratio decreases with decreasing altitude (see Fig. 4), because of the increase in total number density and hence an increase of the rate of the three body reaction (38) and due to the decrease of the HO_2 volume mixing ratio with decreasing altitude.

3.3. Chemical pathways in the upper region

Under global mean conditions, in the upper region, $\hat{\mathscr{P}}_{O_3}$ varies by more than one order of magnitude, whereas $\hat{\Lambda}_{O_3}$ remains relatively constant, suggesting that the O_3 layer is determined by the variation of the O_3 production rate with atmospheric height (see Fig. 5). The major O_3 producing/consuming pathways contributing to these rates are shown in Fig. 6 and Table 2. The rates are considerably larger than the rates of the pathways operating in the lower region (cf. Fig. 3). This provides additional evidence for two distinct chemical regimes in the O_3 chemistry of Mars, indicating an especially active O_3 chemistry in the upper region.

3.3.1. Ozone production (upper region)

As seen in Fig. 5 the O_3 volume mixing ratio profile is strongly affected by the production rate. Our results (Fig. 6) suggest that O_3 production is almost exclusively dominated by the single termolecular recombination reaction (38). Since the $O_2(^3\Sigma)$ and CO_2

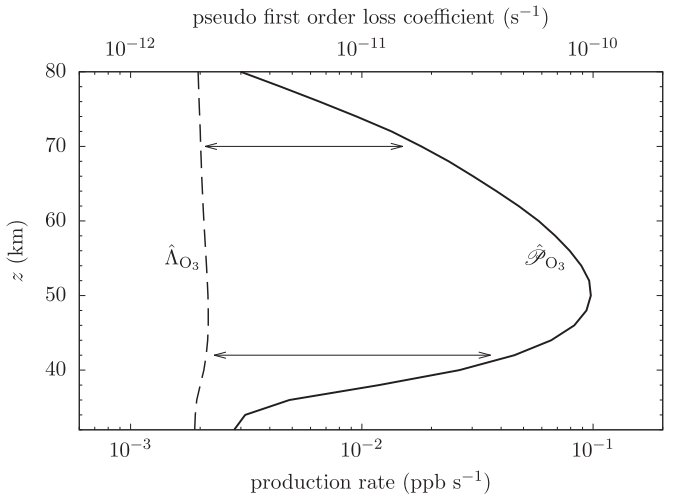

Fig. 5. Ozone production rate (solid line) and pseudo first order O_3 loss rate coefficient (dashed line) calculated according to Eqs. (24) and (30). Since the x-axis is in logarithmic scale, the difference between the solid lines, indicated by the length of the horizontal arrows, describes the ratio $\hat{\mathscr{P}}_{O_3} : \hat{\Lambda}_{O_3}$, which is the volume mixing ratio of O_3 according to Eq. (31).

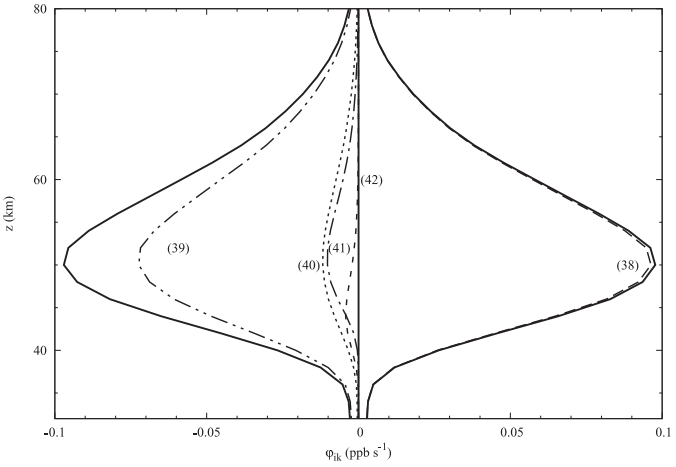

Fig. 6. Rates φ_{ik} of O_3 production/consumption pathways. Loss rates are indicated with a negative sign. The solid line on the right hand side indicates the production of O_3 by all O_3 formation pathways. The solid line on the left hand side indicates the consumption of O_3 by all O_3 consumption pathways. Bracketed numbers refer to pathways given in the text and Table 2.

Table 2
Percentage contribution of the dominant O_3 production and consumption pathways in the mid atmospheric O_3 layer ($z \approx 50$ km).

Production		
(38)	$O(^3P) + O_2(^3\Sigma) + CO_2 \longrightarrow O_3 + CO_2$	**99%**
Consumption		
(39)	$O_3 + h\nu \Longrightarrow O_2(^1\Delta) + O(^3P)$	**75%**
(40)	$O_3 + h\nu \longrightarrow O_2(^3\Sigma) + O(^3P)$	**12%**
(41)	$H + O_3 \longrightarrow OH + O_2(^3\Sigma)$ $O(^3P) + OH \longrightarrow O_2(^3\Sigma) + H$	
Net:	$O_3 + O(^3P) \longrightarrow 2{\cdot}O_2(^3\Sigma)$	**11%**
(42)	$H + O_3 \longrightarrow OH + O_2(^3\Sigma)$ $OH + CO \longrightarrow CO_2 + H$	
Net:	$O_3 + CO \longrightarrow O_2(^3\Sigma) + CO_2$	**2%**

volume mixing ratios remain relatively constant with altitude (see Fig. 1(a)), the strong increase of the $O(^3P)$ volume mixing ratio with increasing altitude leads to an increase in the O_3 production rate and, hence, to an increase in the O_3 volume mixing ratio, which peaks around $z = 50$ km. The decrease of the O_3 production rate with increasing altitude above $z = 50$ km is due to the decrease of the total number density n_{tot} and thus the decrease in the rate of the termolecular reaction (38). The mechanism controlling the $O(^3P)$ abundance in this region is of particular interest, since there $O(^3P)$ is the dominant O_x-species (see Fig. 1(a)). Pathways producing/consuming $O(^3P)$ and their effect on the O_3 profile are discussed in Section 3.3.3.

3.3.2. Ozone consumption (upper region)

Fig. 6 shows also the contributions of O_3 consumption pathways in the upper region. In this part of the atmosphere O_3 is mainly destroyed by photolysis and subsequent thermal deactivation of $O(^1D)$

$$O_3 + h\nu \Longrightarrow O_2(^1\Delta) + O(^3P). \tag{39}$$

A less efficient alternative is the photolysis branch of O_3

$$O_3 + h\nu \longrightarrow O_2(^3\Sigma) + O(^3P), \tag{40}$$

yielding the ground states of molecular $O_2(^3\Sigma)$ and atomic oxygen $O(^3P)$. It is also possible that O_3 is removed by reaction with H via the following two pathways

$$\begin{array}{rrcl} & H + O_3 & \longrightarrow & OH + O_2(^3\Sigma) \\ & O(^3P) + OH & \longrightarrow & O_2(^3\Sigma) + H \\ \text{net:} & O_3 + O(^3P) & \longrightarrow & 2 \cdot O_2(^3\Sigma) \end{array} \tag{41}$$

and

$$\begin{array}{rrcl} & H + O_3 & \longrightarrow & OH + O_2(^3\Sigma) \\ & OH + CO & \longrightarrow & CO_2 + H \\ \text{net:} & O_3 + CO & \longrightarrow & O_2(^3\Sigma) + CO_2, \end{array} \tag{42}$$

which however are less efficient as seen in Fig. 6. For real Mars conditions, the hygropause depends on the season and can rise to higher altitudes during the summer, leading to an increase in the HO_x volume mixing ratio, which in turn, results in the disappearance of the O_3 layer (Clancy and Nair, 1996; Lefèvre et al., 2004). These observations are consistent with our results. Moreover, the presence of ice clouds can reduce the HO_x volume mixing ratio (see e.g. Anbar et al., 1993; Lefèvre et al., 2008), which decreases the rates of pathways (41) and (42) – thus increasing the O_3 volume mixing ratio.

3.3.3. Atomic oxygen production and consumption (upper region)

In contrast to the lower region, in the upper region $O(^3P)$ is more abundant than O_3 (see Fig. 1(a)). In order to understand why $O(^3P)$ is so abundant in this part of the atmosphere, we use the *PAP* algorithm to also study the $O(^3P)$ pathways. Fig. 7 shows the production/consumption of $O(^3P)$ by chemical pathways with and without transport. We denote the $O(^3P)$ production rate by $\hat{\mathcal{P}}^*_{O(^3P)}$ if vertical mixing is included as a pseudo reaction (see Section 2.2) and the pseudo first order $O(^3P)$ loss rate coefficient $\hat{\Lambda}^*_{O(^3P)}$ accordingly. These quantities are related to the chemical $O(^3P)$ production rate and the pseudo first order chemical $O(^3P)$ loss rate coefficient via

$$\hat{\mathcal{P}}^*_{O(^3P)} = \hat{\mathcal{P}}_{O(^3P)} + r^{gain}_{O(^3P)} \tag{43}$$

$$\hat{\Lambda}^*_{O(^3P)} = \hat{\Lambda}_{O(^3P)} + \frac{r^{loss}_{O(^3P)}}{n_{O(^3P)}}, \tag{44}$$

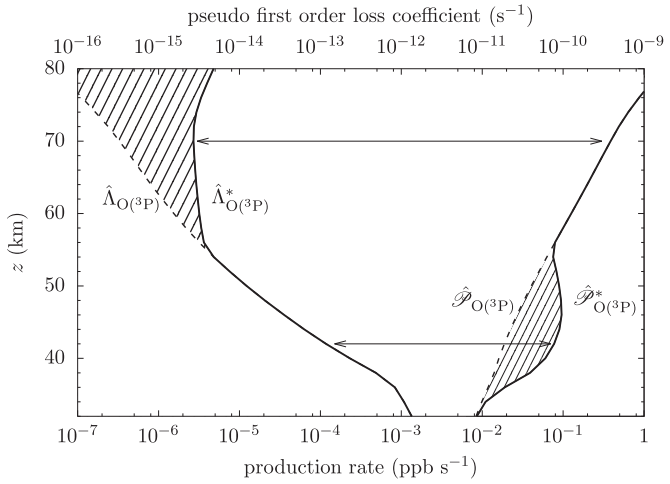

Fig. 7. Pseudo first order $O(^3P)$ loss rate coefficients $\hat{\Lambda}_{O(^3P)}$ and $\hat{\Lambda}^*_{O(^3P)}$ (left branch, upper axis) and $O(^3P)$ production rates $\hat{\mathscr{P}}_{O(^3P)}$ and $\hat{\mathscr{P}}^*_{O(^3P)}$ (right branch, lower axis). Solid lines refer to calculations where vertical transport is included as pseudo reactions according to Eqs. (43) and (44), whereas dashed lines refer to calculations where vertical transport of $O(^3P)$ is not included. Hatched areas illustrate the effect of vertical transport. Since the x-axis is in logarithmic scale, the difference between the solid lines, indicated by the length of the horizontal arrows, describes the ratio $\hat{\mathscr{P}}_{O(^3P)} : \hat{\Lambda}_{O(^3P)}$, which is the volume mixing ratio of $O(^3P)$ according to Eq. (31).

where $r^{gain}_{O(^3P)}$ and $r^{loss}_{O(^3P)}$ are defined by Eqs. (8) and (9). As it can be seen in Fig. 7, there is a net transport of $O(^3P)$ from upper atmospheric layers ($z > 56$ km) to lower altitudes (32 km $\lesssim z \lesssim$ 56 km).

The $O(^3P)$ production rate $\hat{\mathscr{P}}^*_{O(^3P)}$ increases by about one order of magnitude with increasing altitude between $z = 32$ km and $z = 56$ km, whereas the pseudo first order $O(^3P)$ loss rate coefficient $\hat{\Lambda}^*_{O(^3P)}$ decreases by more than two orders of magnitude. This results in an increase of the $O(^3P)$ volume mixing ratio with increasing altitude, which is predominantly determined by the $O(^3P)$ consumption. Fig. 8 shows that the pathways

$$\begin{array}{rrcl} & O(^3P) + HO_2 & \longrightarrow & OH + O_2(^3\Sigma) \\ & OH + CO & \longrightarrow & CO_2 + H \\ & H + O_2(^3\Sigma) + M & \longrightarrow & HO_2 + M \\ \hline \text{net:} & O(^3P) + CO & \longrightarrow & CO_2 \end{array} \qquad (45)$$

and

$$\begin{array}{rrcl} & O(^3P) + OH & \longrightarrow & O_2(^3\Sigma) + H \\ & H + O_2(^3\Sigma) + M & \longrightarrow & HO_2 + M \\ & O(^3P) + HO_2 & \longrightarrow & OH + O_2(^3\Sigma) \\ \hline \text{net:} & 2 \cdot O(^3P) & \longrightarrow & O_2(^3\Sigma) \end{array} \qquad (46)$$

are the most important $O(^3P)$ consumption pathways between $z = 32$ km and $z = 60$ km. Pathway (45) was discussed in the context of the CO_2 stability problem by e.g. McElroy and Donahue (1972); Nair et al. (1994) and Stock et al. (2012a). The rates of both pathways (45) and (46) depend on the abundance of HO_x. The change in the slope of $\hat{\Lambda}_{O(^3P)}$ at $z \approx 36$ km (Fig. 7) correlates with the abrupt decrease in HO_2 volume mixing ratio (Fig. 1(a)), suggesting that a "dry" atmosphere (i.e "lack" of OH and especially HO_2) leads to an increase in the $O(^3P)$ volume mixing ratio. Fig. 8 also suggests that above $z \approx 58$ km, $O(^3P)$ removal via transport dominates. The corresponding pathway includes only the pseudo reaction (7).

Atomic oxygen $O(^3P)$ is produced directly by CO_2 photolysis

$$CO_2 + h\nu \quad \Longrightarrow \quad CO + O(^3P) \qquad (47)$$

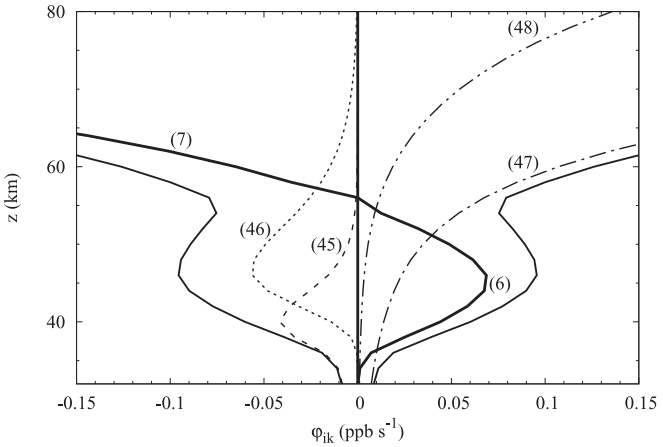

Fig. 8. Rates φ_{ik} of $O(^3P)$ production/consumption pathways. Loss rates are indicated with a negative sign. The solid line on the right hand side indicates the production of $O(^3P)$ by all $O(^3P)$ formation pathways. The solid line on the left hand side indicates the consumption of $O(^3P)$ by all $O(^3P)$ consumption pathways. The thick solid lines on the refer to the transport pathways (6) and (7). Pathways are summarized in Table 3.

Table 3
Percentage contribution of the dominant $O(^3P)$ production and consumption pathways in the mid atmospheric O_3 layer ($z \approx 50$ km).

Production		
(6)	$O(^3P)$[adjacent layer(s)] $\longrightarrow$ $O(^3P)$	**55%**
(47)	$CO_2 + h\nu \Longrightarrow CO + O(^3P)$	**39%**
(48)	$O_2(^3\Sigma) + h\nu \Longrightarrow O(^3P) + O(^3P)$	**6%**
Consumption		
(45)	$O(^3P) + HO_2 \longrightarrow OH + O_2(^3\Sigma)$ $OH + CO \longrightarrow CO_2 + H$ $H + O_2(^3\Sigma) + M \longrightarrow HO_2 + M$	
Net:	$O(^3P) + CO \longrightarrow CO_2$	**55%**
(46)	$O(^3P) + OH \longrightarrow O_2(^3\Sigma) + H$ $H + O_2(^3\Sigma) + M \longrightarrow HO_2 + M$ $O(^3P) + HO_2 \longrightarrow OH + O_2(^3\Sigma)$	
Net:	$2{\cdot}O(^3P) \longrightarrow O_2(^3\Sigma)$	**23%**

and O_2 photolysis

$$O_2(^3\Sigma) + h\nu \quad \Longrightarrow \quad O(^3P) + O(^3P) \qquad (48)$$

$O(^3P)$ is then transported downwards to the O_3 layer of the upper region. The corresponding pathway includes only the pseudo reaction (6). In order to illustrate the effect of vertical transport of $O(^3P)$ on the O_3 profile, we calculate first the concentration profiles of $O(^3P)$ in the absence of $O(^3P)$ transport, i.e.

$$n^{\circ}_{O(^3P)} = \frac{\hat{\mathcal{P}}_{O(^3P)}}{\hat{\Lambda}_{O(^3P)}}. \qquad (49)$$

Note that $\hat{\mathcal{P}}_{O(^3P)}$ and $\hat{\Lambda}_{O(^3P)}$ do not include the transport pseudo reactions (6) and (7). Fig. 9(a) shows that vertical transport leads to an increase in $O(^3P)$ volume mixing ratio below $z = 56$ km and a decrease above $z = 56$ km consistent with Fig. 7. This indicates that $O(^3P)$ is effectively transported downwards. To estimate the effect of $O(^3P)$ transport on the O_3 profile, we use $n^{\circ}_{O(^3P)}$ from Eq. (49), in order to derive a hypothetical O_3 profile that would be formed in the absence of $O(^3P)$ transport. Fig. 6 suggests that we can approximate $\hat{\mathcal{P}}_{O_3}$ by r_{38}. We use the modified concentration $n^{\circ}_{O(^3P)}$, when computing the rate of reaction (38), henceforth called r°_{38}, i.e. we

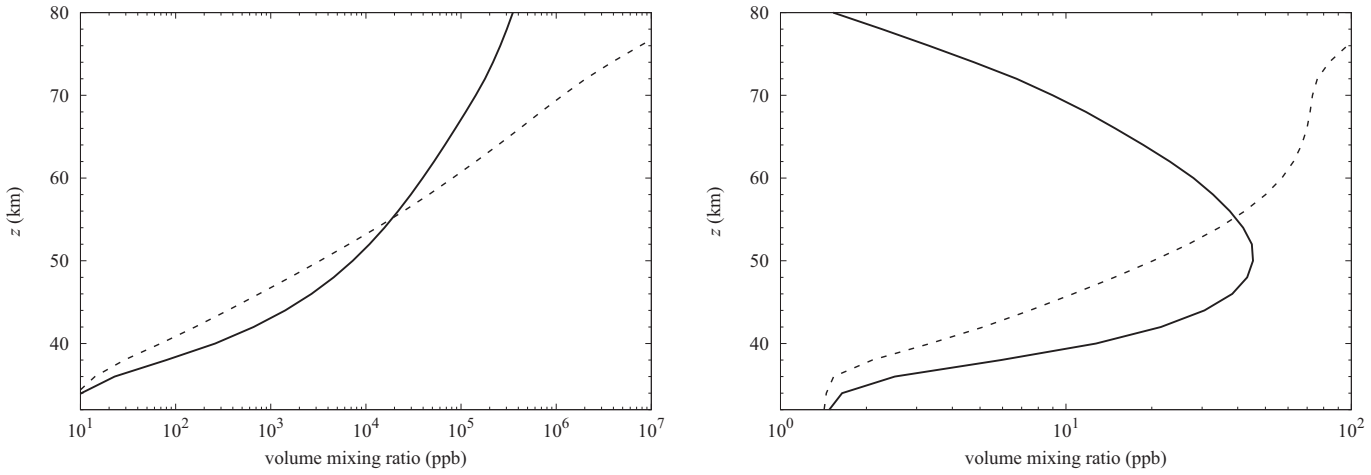

(a) Ground state atomic oxygen. (b) Ozone.

Fig. 9. Volume mixing ratios of $O(^3P)$ and O_3. Solid lines indicate the profiles calculated by the Caltech/JPL KINETICS model. Dashed lines refer to the volume mixing ratio profiles n_i°/n_{tot} estimated in the absence of $O(^3P)$ transport.

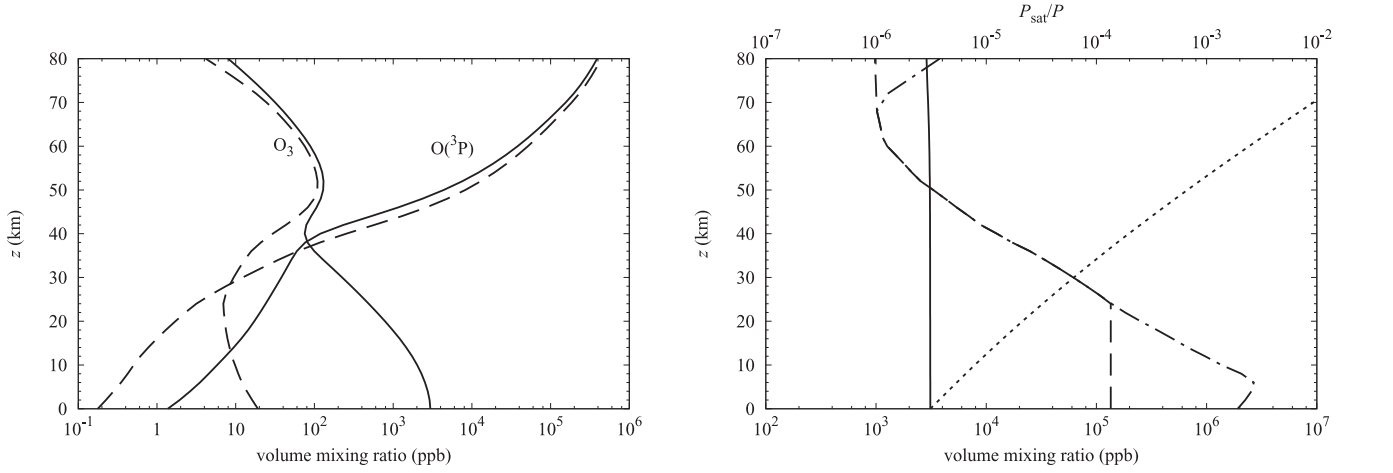

(a) Odd oxygen ($O(^3P)$, O_3). (b) Water vapor and the ratio of the saturation pressure of H_2O and the atmospheric pressure.

Fig. 10. Volume mixing ratios of selected species in the Martian atmosphere calculated by the Caltech/JPL KINETICS model. Solid lines refer to the scenario with the modified temperature profile (see text), dashed lines refer to the "standard" scenario. Dotted line (right hand panel) refer to the ratio P_{sat}:P (modified temperature profile), dot-dashed line refer to the ratio P_{sat}:P ("standard" scenario).

exclude the effect of $O(^3P)$ transport without modifying the transport of other chemical species. $\hat{\Lambda}_{O_3}$ depends on $O(^3P)$ transport via pathway (41). Since, however, the rate of pathway (41) is considerably smaller than the rates of pathways (39) and (40), $O(^3P)$ transport can be neglected in the calculation of $\hat{\Lambda}_{O_3}$. Nonetheless, $O(^3P)$ transport can affect the OH-abundance via reaction (37), which in turn may influence the rates of the O_3 consumption pathways (41) and (42). This effect is expected to be relatively small in comparison to the direct influence of $O(^3P)$ transport on $\hat{\mathcal{P}}_{O_3}$ (see Fig. 6.). The hypothetical O_3 profile – without $O(^3P)$ transport – can then be calculated via

$$n^\circ_{O_3} \approx \frac{r^\circ_{38}}{\hat{\Lambda}_{O_3}}. \tag{50}$$

Fig. 9(b) suggests that $O(^3P)$ transport has two effects on the vertical O_3 profile. Firstly, we find a larger O_3 volume mixing ratio below $z = 56$ km and a smaller O_3 volume mixing ratio above $z = 56$ km. Secondly, vertical transport of $O(^3P)$ is essential for the formation of the local O_3 maximum in the investigated altitude range. Since vertical transport of $O(^3P)$ depends on the eddy diffusion profile, we expect, in accordance with McElroy and Donahue (1972) and Parkinson and Hunten (1972), the O_3 profile to be sensitive to the eddy diffusion profile.

3.4. Effect of the temperature profile on the O_3 layer

Reaction rate coefficients and the saturation pressure of H_2O are functions of temperature and inevitably affect the reaction rates in the chemical network. Hence, the HO_x abundance, and consequently, the O_3 volume mixing ratio profile depend implicitly on temperature. Therefore, it might be theoretically possible that the characteristic O_3 profile on Mars is mainly a consequence of a specific atmospheric temperature profile.

To investigate this effect, we calculate the volume mixing ratios using an *idealized* temperature profile, which is constant ($T_{\text{av}} = 176.5$ K) up to $z = 136$ km and then follows our standard temperature profile adopted from Nair et al. (1994). The value T_{av} is the arithmetic mean of the surface temperature and the mini-

mum temperature in the standard case. The lower altitude atmospheric temperature causes a larger amount of H_2O to condense, resulting in less HO_x. Hence the O_3 abundance increases by about two orders of magnitude (see Fig. 10(a)). In the upper region the modified temperature profile has no significant effect on the H_2O and O_3 abundances and the O_3 profile, i.e. the mid-atmospheric O_3 layer still exists (see Fig. 10(a) and (b)). This means that the change in temperature with altitude is not responsible for the formation of the O_3 layer.

4. Conclusions

We provide the first quantitative pathway analysis of the Martian atmospheric O_3 profile by applying the *Pathway Analysis Program (PAP)* for the first time to the output of the updated JPL/Caltech KINETICS model in order to gain a better understanding of the relevant chemical and transport processes and therefore also a better understanding of observable features. From inspection of the concentrations of $O(^3P)$ and O_3 and as a result of our analysis, the Martian atmosphere can be divided into two chemically distinct regions. In the lower region, the dominant O_x species is O_3 and in the upper region the dominant O_x species is $O(^3P)$. These regions differ significantly in the manner in which processes control the O_3 abundance.

The pathway analysis confirms, that in the lower region, O_3 is formed by a Chapman-like mechanism, involving CO_2 photolysis (instead of O_2 photolysis as on Earth), which is consistent with earlier findings by e.g McElroy and Donahue (1972). On Mars O_3 consumption proceeds via pathways involving HO_x. The decrease of the total O_3 loss rate coefficient with decreasing altitude leads to the formation of the ground layer O_3 maximum. Most of the O_3, destroyed via photolysis, is recycled back.

In the upper region, $O(^3P)$ is the dominant O_x species. Therefore, we further analyzed $O(^3P)$ production and consumption between $z \approx 32$ km and $z \approx 80$ km. The additional *PAP* analysis shows in accordance with Parkinson and Hunten (1972) and Krasnopolsky (1993) that the main reason for the high abundance of $O(^3P)$ is the small concentration of OH and HO_2 above $z \approx 35$ km altitude. In the upper region O_3 is produced by one reaction, namely $O(^3P) + O_2(^3\Sigma) + CO_2 \longrightarrow O_3 + CO_2$, which critically depends on the downward transport of $O(^3P)$ from upper atmospheric layers ($z > 56$ km) into the Martian O_3 layer. There, O_3 is mainly removed by photolysis and to some part by reaction with H, which is subsequently recycled. Although clearly, O_3 consumption pathways are important to regulate the absolute abundance of O_3, the shape of the O_3 profile is mainly determined by the O_3 production mechanism. The increase of the O_3 volume mixing ratio below $z = 50$ km is due to the strong increase of $O(^3P)$ with increasing altitude, which in turn can be explained by the decreasing concentration of OH and HO_2. The decrease of the O_3 volume mixing ratio with increasing altitude above $z = 50$ km is a result of the decreasing rate of the termolecular reaction $O(^3P) + O_2(^3\Sigma) + CO_2 \longrightarrow O_3 + CO_2$.

Recent observations (Clancy et al., 2013; Rezac et al., 2015; Villanueva et al., 2013) demonstrate that many of the species relevant for the O_3 chemistry (OH, O, HO_2) are now detectable. To improve our understanding of the Martian atmospheric O_3 profile, simultaneous measurements of these species in combination with H_2O and O_3 would be desirable.

Acknowledgment

This research has been partly supported by the Helmholtz Association through the research alliance “Planetary Evolution and Life”. This work was partially funded by grant AyA 2012–32237 awarded by the Spanish Ministerio de Economia y Competitividad. The authors would like to thank Run-Lie Shia and Dickens Saint-Hilaire for their contributions to the discussion.

References

Anbar, A.D., Leu, M.-T., Nair, H.A., Yung, Y.L., 1993. Adsorption of HO_x on aerosol surfaces: implications for the atmsophere of Mars. J. Geophy. Res. 98, 10933–10940.
Anderson, E., Leovy, C., 1978. Mariner 9 television limb observations of dust and ice hazes on Mars. J. Atmos. Sci. 35, 723–734.
Atreya, S.K., Gu, Z.G., 1994. Stability of the martian atmosphere: is heterogeneous catalysis essential? J. Geophy. Res. 99, 13133–13145.
Barker, E.S., 1976. Martian atmospheric water vapor observations – 1972-74 apparition. Icarus 28, 247–268.
Barth, C.A., Hord, C.W., 1971. Mariner ultraviolet spectrometer: topography and polar cap. Science 173, 197–201.
Barth, C.A., Hord, C.W., Stewart, A.I., Lane, A.L., Disk, M.L., Anderson, G.P., 1973. Mariner 9 ultraviolet spectrometer experiment: seasonal variations of ozone on Mars. Science 179, 795–796.
Bates, D.R., Nicolet, M., 1950. The photochemistry of atmospheric water vapour. J. Geophys. Res. 55, 301–327.
Bertaux, J.-L, Fonteyn, D., Korablev, O., Chassefière, E., Dimarellis, E., Dubois, J.P, Hauchecorne, A., Cabane, M., Rannou, P., Levasseur-Regourd, A.C, Cernogora, G., Quemerais, E., Hermans, C., Kockarts, G., Lippens, C., Maziere, M. De, Moreau, D., Muller, C., Neefs, B., Simon, P.C, Forget, F., Hourdin, F., Talagrand, O., Moroz, V.I, Rodin, A., Sandel, B., Stern, A., 2000. The study of the Martian atmsophere from top to bottom with SPICAM light on Mars Express. Planet. Space Sci. 48, 1303–1320.
Bertaux, J.-L., Korablev, O., Perrier, S., Quémerais, E., Montmessin, F., Leblanc, F., Lebonnois, S., Rannou, P., Lefèvre, F., Forget, F., Fedorova, A., Dimarellis, E., Reberac, A., Fonteyn, D., Chaufray, J.Y., Guibert, S., 2006. SPICAM on Mars Express: observing modes and overview of UV spectrometer data and scientific results. J. Geophys. Res. 111, E10S90.
Blamont, J.E., Chassefière, E., 1993. First detection of ozone in the middle atmosphere of Mars from solar occultation measurements. Icarus 104, 324–336.
Boxe, C.S, Francisco, J.S, Shia, R.-L., Yung, Y.L, Nair, H., Liang, M.-C., Saiz-Lopez, A., 2014. New insights into martian atmospheric chemistry. Icarus 242, 97–104.
Brasseur, G.P., Orlando, J., Tyndall, G., 1999. Atmospheric Chemistry and Global Change. Oxford University Press, New York.
Chassefière, E., Blamont, J.E., Krasnopolsky, V.A., Korablev, O.I., Atreya, S.K., West, R.A., 1992. Vertical structure and size distributions of martian aerosols from solar occultation measurements. Icarus 97, 46–69.
Clancy, R.T, Sandor, B.J, García-Muñoz, A., Lefèvre, F., Smith, M.D, Wolff, M.J, Montmessin, F., Murchie, S.L, Nair, H., 2013. First detection of Mars atmospheric hydroxyl: CRISM near-IR measurement versus LMD GCM simulation of OH meinel band emission in the Mars polar winter atmosphere. Icarus 226, 272–281.
Clancy, R.T., Nair, H., 1996. Annual (perihelion-aphelion) cycles in the photochemical behavior of the global Mars atmosphere. J. Geophys. Res. 101, 12785–12790.
Clancy, R.T., Wolff, M.J., Lefèvre, F., Cantor, B.A., Malin, M.C., Smith, M.D., 2016. Daily global mapping of Mars ozone column abundances with MARCI UV band imaging. Icarus 266, 112–133.
Crutzen, P.J., 1970. The influence of nitrogen oxides on the atmospheric ozone content. Quart. J. R. Met. Soc. 96, 320–325.
Espenak, F., Mumma, M.J., Kostiuk, T., Zipoy, D., 1991. Ground-based infrared measurements of the global distribution of ozone in the atmosphere of Mars. Icarus 92, 252–262.
Fast, K., Kostiuk, T., Espenak, F., Annen, J., Buhl, D., Hewagama, T., A'Hearn, M.F, Zipoy, D., Livengood, T.A, Sonnabend, G., Schmülling, F., 2006a. Ozone abundance on Mars from infrared heterodyne spectra I. Acquisition, retval, and anticorrelation with water vapor. Icarus 181, 431–491.
Fast, K., Kostiuk, T., Hewagama, T., A'Hearn, M.F, Livengood, T.A, Lebonnois, S., Lefèvre, F., 2006b. Ozone abundance on Mars from infrared heterodyne spectra II. Validating photochemical models. Icarus 183, 396–402.
Grenfell, J., Lehmann, R., Mieth, P., Langematz, U., Steil, B., 2006. Chemical reaction pathways affecting stratospheric and mesospheric ozone. J. Geophy. Res. 111, D17311.
Grenfell, J.L., Gebauer, S., Godolt, M., Palczynski, K., Rauer, H., Stock, J., von Paris, P., Lehmann, R., Selsis, F., 2013. Potential biosignatures in super-earth atmospheres II. Photochemical responses. Astrobiology. 13, 415–438.
Houben, H., Haberle, R.M., Young, R.E., Zent, A.P., 1997. Modeling the martian seasonal water cycle. J. Geophy. Res. 102, 9069–9084.
Jacobson, M.Z., 2005. Fundamentals of Atmospheric Modeling. Cambridge University Press, New York.
Jakosky, B.M., 1985. The seasonal cycle of water on Mars. Space Sci. Rev. 41, 131–200.
Jakosky, B.M., Farmer, C.B., 1982. The seasonal and global behavior of water vapor in the Mars atmosphere – complete global results of the viking atmospheric water detector experiment. J. Geophy. Res. 87, 2999–3019.
Korablev, O.I., Krasnopolsky, V.A., Rodin, A.V., Chassefière, E., 1993. Vertical structure of martian dust measured by solar infrared occultations from the *Phobos* spacecraft. Icarus 102, 76–87.
Krasnopolsky, V.A., 1993. Photochemistry of the martian atmsophere (mean conditions). Icarus 101, 313–332.

Krasnopolsky, V.A., 2003. Mapping of Mars o_2 1.27-μm dayglow at four seasonal points. Icarus 165, 315–325.
Krasnopolsky, V.A., Bjoraker, G.L., 2000. Mapping of Mars $O_2(^1\Delta)$ dayglow. J. Geophys. Res. 105 (E8), 20179–20188.
Krasnopolsky, V.A., Krysko, A.A., Rogachev, V.N., 1975. Measurement of ozone in a planetary atmosphere by space probe Mars-5. In: Kosmicheskie Issledovaniia., Vol. 13, pp. 37–41. (translation: Cosmic Research. 13, 31–34.)
Krasnopolsky, V.A., Parshev, V.A., 1979. Ozone and photochemistry of the martian lower atmosphere. Planet. Space Sci. 27, 113–120.
Lane, A.L., Barth, C.A., Hord, C.W., Stewart, A.I., 1973. Mariner 9 ultraviolet spectrometer: observations of ozone on Mars. Icarus 18, 102–108.
Lebonnois, S., Quémerais, E., Montmessin, F., Lefèvre, F., Perrier, S., Bertaux, J.-L., Forget, F., 2006. Vertical distribution of ozone on Mars as measured by SPICAM/Mars express using stellar occultations. J. Geophys. Res. 111, E09S06.
Lefèvre, F., et al., 2008. Heterogeneous chemistry in the atmosphere of Mars. Nature 454, 971–975.
Lefèvre, F., Lebonnois, S., Montmessin, F., Forget, F., 2004. Three-dimensional modeling of ozone on Mars. J. Geophys. Res. 109, E07004.
Lehmann, R., 2004. An algorithm for the determination of all significant pathways in chemical reaction systems. J. Atmos. Chem. 47, 45–78.
Matsumi, Y., Comes, F.J., Hancock, G., Hofzumahaus, A., Hynes, A.J., Kawasaki, M., Ravishankara, A.R., 2002. Quantum yields for production of $o(^1D)$ in the ultraviolet photolysis of ozone: recommendation based on evaluation of laboratory data. J. Geophys. Res. 107 (D3), 2156–2202.
McElroy, M.B., Donahue, T.M., 1972. Stability of the martian atmosphere. Science 177, 986–988.
Montmessin, F., Forget, F., Rannou, P., Cabane, M., Haberle, R.M., 2004. Origin and role of water ice clouds in the martian water cycle inferred from a general circulation model. J. Geophys. Res. 109, E10004.
Nair, H., Allen, M., Anbar, A.D., Yung, Y.L., 1994. A photochemical model of the martian atmosphere. Icarus 111, 124–150.
Novak, R.E., Mumma, M.J., DiSanti, M.A., Dello Russo, N., 2002. Mapping of ozone and water in the atmosphere of Mars near the 1997 aphelion. Icarus 158, 14–23.
Noxon, J.F., Traub, W.A., Carleton, N.P., Connes, P., 1976. Detection of o_2 dayglow emission from Mars and the martian ozone abundance. Astrophys. J. 207, 1025–1035.
Parkinson, T.M., Hunten, D.M., 1972. Spectroscopy and aeronomy of o_2 on Mars. J. Atmos. Sci. 29, 1380–1390.
Perrier, S., Bertaux, J. L., Lefèvre, F., Lebonnois, S., Korablev, O., Fedorova, A., Montmessin, F., 2006. Global distribution of total ozone on Mars from SPICAM/MEX UV measurements. J. Geophy. Res. 111, E09S06.
Rezac, L., Hartogh, P., Güsten, R., Wiesemeyer, H., Hübers, H.-W., Jarchow, C., Richter, H., Klein, B., Honingh, N., 2015. First detection of the 63 μm atomic oxygen line in the thermosphere of Mars with GREAT/SOFIA. Astron. Astrophys. 580, L10.
Richardson, M.I., Wilson, R.J., 2002. Investigation of the nature and stability of the martian seasonal water cycle with a general circulation model. J. Geophy. Res. (Planets) 107, E55031.
Rosenqvist, J., Chassefière, E., 1995. A reexamination of the relationship between eddy mixing and o_2 in the martian middle atmosphere. J. Geophy. Res. 100, 5541–5551.
Sander, S.P., Abbatt, J., Barker, J.R., Burkholder, J.B., Friedl, R.R., Golden, D.M., Huie, R.E., Kolb, C.E., Kurylo, M.J., Moortgat, G.K., Orkin, V.L., Wine, P.H., 2011. Chemical kinetics and photochemical data for use in atmospheric studies. In: Evaluation number 17, JPL Publ., pp. 10–16.
Smith, M.D., 2004. Interannual variability in TES atmospheric observations of Mars during 1999–2003. Icarus 167, 148–165.
Stock, J.W, Boxe, C.S, Lehmann, R., Grenfell, J.L, Patzer, A.B.C., Rauer, H., Yung, Y.L., 2012a. Chemical pathway analysis of the Martian atmosphere: CO_2-formation pathways. Icarus 219, 13–14.
Stock, J.W., Grenfell, J.L., Lehmann, R., Patzer, A.B.C., Rauer, H., 2012b. Chemical pathway analysis of the lower martian atmosphere: the CO_2 stability problem. Planet. Space Sci. 68, 18–24.
Toon, O.B., Pollack, J.B., Sagan, C., 1977. Physical properties of the particles composing the martian dust storm of 1971–1972. Icarus 30, 663–696.
Traub, W.A., Carleton, N.P., Connes, P., Noxon, J.F., 1979. The latitude variation of o_2 dayglow and o_3 abundance on Mars. Astrophys. J. 229, 846–854.
Verronen, P.T., Lehmann, R., 2013. Analysis and parameteriation of ionic reactions affecting middleatmospheric HO_x and NO_x during solar proton events. Annales Geophysicae 31, 909–956.
Verronen, P.T., Lehmann, R., 2015. Enhancement of odd nitrogen modifies mesospheric ozone chemistry during polar winter. Geophys. Res. Lett. 42, 10445–10452.
Verronen, P.T., Santee, M.L., Manney, G.L., Lehmann, R., Salmi, S.-M., Seppälä, A., 2011. Nitirc acid enhancements in the mesosphere during january 2005 and december 2006 solar proton events. J. Geophy. Res. 116, D17301.
Villanueva, G.L, Mumma, M.J, Novak, R.E, Radeva, Y.L, Käufl, H.U., Smette, A., Tokunaga, A., Khayat, A., Encrenaz, T., Hartogh, P., 2013. A sensitive search for organics (CH_4, CH_3OH, H_2CO, C_2H_6, C_2H_2, C_2H_4), hydroperoxyl (HO_2), nitrogen compounds (N_2O, NH_3, HCN) and chlorine species (HCl, CH_3Cl) on Mars using ground-based high-resolution infrared spectroscopy. Icarus 223, 11–27.
Yung, Y.L., DeMore, W.B., 1999. Photochemistry of Planetary Atmospheres. Oxford University Press, New York.